

JGR Atmospheres

RESEARCH ARTICLE

10.1029/2021JD036007

Key Points:

- Simulations of the migrating semidiurnal (SW2) tide are validated against observations from a high-latitude array of Super Dual Auroral Radar Network meteor radars
- Numerical experiments investigate the impact of the background atmosphere, tidal dissipation, and tidal forcing on the simulation results
- The simulated SW2 is largely shaped by the background atmosphere, while being sensitive to eddy diffusion and surface friction

Correspondence to:

W. E. van Caspel,
willem.e.v.caspel@ntnu.no

Citation:

van Caspel, W. E., Espy, P. J., Ortland, D. A., & Hibbins, R. E. (2022). The mid- to high-latitude migrating semidiurnal tide: Results from a mechanistic tide model and SuperDARN observations. *Journal of Geophysical Research: Atmospheres*, 127, e2021JD036007. <https://doi.org/10.1029/2021JD036007>

Received 8 OCT 2021
Accepted 30 DEC 2021

The Mid- to High-Latitude Migrating Semidiurnal Tide: Results From a Mechanistic Tide Model and SuperDARN Observations

Willem E. van Caspel^{1,2} , Patrick J. Espy^{1,2} , David A. Ortland³ , and Robert E. Hibbins^{1,2} 

¹Department of Physics, Norwegian University of Science and Technology (NTNU), Trondheim, Norway, ²Birkeland Centre for Space Science, Bergen, Norway, ³Northwest Research Associates, Inc., Redmond, WA, USA

Abstract Simulations of the solar thermal migrating semidiurnal (SW2) tide in the mesosphere-lower-thermosphere (MLT) are compared against meteor wind observations from a longitudinal chain of high-latitude Super Dual Auroral Radar Network radars. The simulations span the year 2015 and are performed using a mechanistic primitive equation model. The model employs a whole-atmosphere tide forcing based on temperature tendency fields from the Specified Dynamics Whole Atmosphere Community Climate Model with Thermosphere and Ionosphere Extension, and a background atmospheric specification based on zonal wind and temperature data from the Navy Global Environmental Model-High Altitude meteorological analysis system. Results show that the model accurately reproduces the observed seasonal variability of the SW2 tide in both the amplitude and phase. Numerical experiments are performed to investigate how the tidal forcing, dissipation terms, and seasonal variations in the background atmosphere shape the seasonal variations of the simulated SW2 tide. Notable results are that the background atmosphere most strongly impacts the SW2 tide forced in the troposphere, and that the specification of a narrow surface friction profile enhances the net SW2 amplitude in the MLT between April and October. Eddy diffusion is found to damp the simulated tide predominantly around summer solstice and in December.

1. Introduction

Atmospheric tides are global-scale waves whose periods are an integer fraction of a solar day (Chapman & Lindzen, 1970). The tides are forced primarily by radiative and latent heating effects in the lower atmosphere (Hagan, 1996), but obtain their largest amplitudes in the mesosphere-lower-thermosphere (MLT) region (80–120 km altitude). There they are expressed as pronounced oscillations in a broad range of atmospheric fields, such as density, pressure, and wind. The migrating tides are those tides which follow the apparent motion of the sun, having a longitudinal zonal wavenumber (S) and latitudinal spherical harmonic (Hough mode) structure. In the current work, the focus lies on the migrating semidiurnal (SW2; for Semidiurnal, Westward $S = 2$) tide. The SW2 tidal winds maximize in the mid- and high-latitude MLT (Manson et al., 2002; Wu et al., 2011), where they form a major source of day-to-day and inter-seasonal variability of the MLT-ionosphere system (Arras et al., 2009; G. Shepherd et al., 1998; Smith, 2012). The SW2 tide is recognized as an important vertical coupling mechanism (Forbes, 2009; Pedatella & Forbes, 2010), and as a contributing factor to the vertical mixing and energy budget of the upper atmosphere (Becker, 2017; Forbes et al., 1993).

The numerical study of the SW2 tide has a long history (e.g., Forbes & Garrett, 1979). Nevertheless, open questions remain about the mechanisms governing the tide's seasonal and short-term variability (Conte et al., 2018; G. Liu et al., 2021; Pedatella et al., 2020; Zhang et al., 2021). Many recent studies are in part driven by the increasing availability of high-altitude and tide-resolving general circulation models. A challenging aspect of using such models is that the representation of the SW2 tide can vary significantly from model to model (McCormack et al., 2021; Pancheva et al., 2020; Stober et al., 2021), while the cause of these differences is often obscured by the complexity of the models.

In the current work, a development of the mechanistic tide model from Ortland (2017) is used to simulate the SW2 tide observed in the MLT by a longitudinal array of Super Dual Auroral Radar Network (SuperDARN) meteor radars. The purpose of the simulations is to mechanistically identify which processes contribute to the seasonal variations of the SW2 tide in the mid- to high-latitude MLT. To this end, the model employs a realistic background atmosphere based on zonal mean zonal winds and temperatures from the Navy Global Environmental

Model-High Altitude (NAVEM-HA), and a whole-atmosphere tidal forcing based on heating rates from the Specified Dynamics Whole Atmosphere Community Climate Model with Thermosphere Extension (SD-WAC-CMX). Dissipative processes are parameterized between the surface and thermosphere, which includes a specification of ion drag, Newtonian cooling, surface friction, and a seasonally dependent eddy diffusion.

Section 2 discusses the model and data used in this work. This includes a description of the model configuration, its dissipation terms, tidal forcing scheme, background atmospheric specification, and output analysis. In Section 3, the simulated SW2 tidal amplitude and phase are validated against observation for the year 2015, with reference to climatological observations. Section 4 describes a series of numerical experiments investigating how the background atmosphere, tidal forcing, and dissipation terms shape the seasonal variations of the simulated SW2 tide. In Section 5, the impact of the background atmosphere is investigated in more detail, where a distinction is made between the SW2 tide forced in the troposphere, stratosphere, and mesosphere-thermosphere (MT) regions. A discussion of the results is given in Section 6.

2. Data and Model Description

2.1. Primitive Equation Model

The model is a development of the primitive equations in sigma-coordinates model (PRISM) described in detail in Ortland (2017) and references therein. Earlier works have used the model to study tide-gravity wave interactions (Ortland & Alexander, 2006), tropical waves (Ortland & Alexander, 2014; Ortland et al., 2011), planetary waves (Lieberman et al., 2021), and tide-planetary wave interactions (Lieberman et al., 2015). PRISM is a three-dimensional nonlinear and time-dependent spectral model, which numerically integrates the vorticity and divergence form of the primitive equations. For a comprehensive discussion of the primitive equations, the reader is referred to Holton (2003).

In the current work, PRISM is configured to have 121 vertical levels between the surface and 7.5×10^{-6} Pa (~ 430 km altitude), with a vertical grid spacing of approximately 0.1 km in the troposphere and 2.0 km in the MLT. A realistic surface topography is included by incorporating the surface geopotential field from the European Centre for Medium-Range Weather Forecasts (ECMWF) ERA5 reanalysis model (Hersbach et al., 2020). The horizontal resolution of PRISM is truncated at zonal wavenumber $S = 3$ and associated Legendre polynomial of degree $N = 23$, while a step size of $\Delta t = 0.3$ hr is used in the semi-implicit time-integration scheme. Higher order horizontal, vertical, or temporal resolutions were found to have very little impact on the simulated SW2 tide. No parameterization of gravity waves is included in the current work.

2.2. Dissipation

The model employs a number of one-dimensional vertical dissipation profiles, which act to damp the vorticity (ξ), divergence (D), and temperature (Θ) fields. Damping is achieved by subtracting the model state at time-step $n-1$ to the tendency equation at time-step n at each of the model levels l , as

$$\frac{\partial \chi_l^n}{\partial t} = \dots - \nu_l \chi_l^{n-1}; \quad \chi_l = \xi_l, D_l, \Theta_l, \quad (1)$$

where ν_l represents the dissipation coefficients in units of s^{-1} , and where the three dots represent the model tendency equation without damping. Figure 1 gives an overview of the dissipation terms used in this study, where the coefficients have been scaled to units of $days^{-1}$ (d^{-1}).

A parameterization of ion drag, represented by a Rayleigh friction acting on the vorticity and divergence fields, is included to crudely represent the exchange of momentum between neutral molecules and ions moving under the influence of Earth's magnetic field. The coefficients of ion drag (ν_i) follow those calculated by Hong and Lindzen (1976) for solar maximum conditions, using the expression $\nu_i(z) = 10^{-4} \times \tanh [(z - 110)/30] s^{-1}$ with z in units of kilometer. Damping due to radiative cooling by CO_2 and O_3 in the troposphere and stratosphere is parameterized as a Newtonian cooling. The Newtonian cooling profile broadly follows those from Hagan et al. (1993) and Wood and Andrews (1997), and reduces to a value of zero above 70 km altitude.

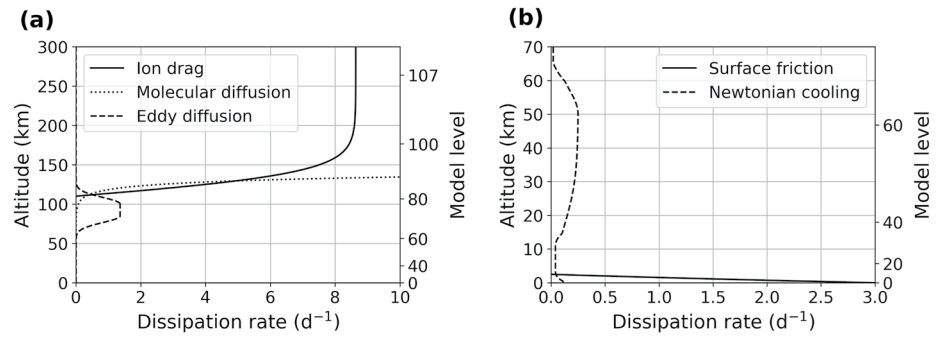


Figure 1. Vertical profiles of the coefficients of ion drag, molecular diffusion, and peak eddy diffusion (a), and the vertical profiles of the surface friction and Newtonian cooling coefficients (b).

Following Vial (1986) (hereafter V86) and others (e.g., Forbes & Vincent, 1989; Wood & Andrews, 1997), vertical eddy diffusion of momentum is parameterized as an effective Rayleigh friction. For a wave with vertical wavenumber k_z this approximation is written as

$$v_{\text{eff},t} = K_t k_z^2, \quad (2)$$

where K_t ($\text{m}^2 \text{s}^{-1}$) represents eddy diffusion and $v_{\text{eff},t}$ is the corresponding effective Rayleigh friction coefficient. Following V86, a value of $k_z = 2\pi/25 \text{ km}^{-1}$ is adopted for the simulation of the semidiurnal tide. This wavelength is characteristic of the semidiurnal (2, 5) Hough mode, which is the lowest order Hough mode which is expected to be affected by dissipation at meteor echo altitudes. Lower order Hough modes are typically only weakly affected by dissipation, owing to their longer vertical wavelengths (Forbes & Garrett, 1979).

The notation of V86 is adopted for a vertical profile of eddy diffusion, which is written as

$$K_t(z) = \begin{cases} K_0 \exp[-((z - z_1)/a_1)^2], & z \leq z_1 \\ K_0, & z_1 \leq z \leq z_2 \\ K_0 \exp[-((z - z_2)/a_2)^2], & z \geq z_2, \end{cases} \quad (3)$$

where z is in units of kilometer. While V86 considers values in the range of $z_1 = 91.7\text{--}96.6 \text{ km}$, $z_2 = 100.1\text{--}102.9 \text{ km}$, $a_1 = 7.7\text{--}8.4 \text{ km}$, and $a_2 = 7.8 \text{ km}$, the current work adopts the values of $z_1 = 85 \text{ km}$, $z_2 = 100 \text{ km}$ and $a_1 = a_2 = 12 \text{ km}$. These values yield a vertical profile that is representative of a seasonal mid- and high-latitude

average based on the Garcia and Solomon (1985) model, whose vertical and latitudinal variations are illustrated in more detail in Hagan et al. (1995). The mid- and high-latitude vertical profile of the Garcia and Solomon (1985) model is generally broader than that of V86, reaching its highest dissipation rates between 70 and 110 km altitude depending on season.

The K_0 -term in Equation 3 controls the magnitude of the eddy diffusion profile, and for this the eddy diffusion coefficient specified at the lower boundary ($\sim 97 \text{ km}$ altitude) of the Thermosphere-Ionosphere-Electrodynamics General Circulation Model by Qian et al. (2009) (hereafter Q09) is used. A key feature of the K_0 from Q09 is that it follows the seasonal variations in global eddy diffusion, as inferred from satellite drag and O/N_2 observations. The eddy diffusion itself is attributed to seasonal variations in the mixing caused by dissipating gravity waves. In the current work, however, the seasonal variations of Q09 are shifted forward in time by 30 days. The effect of this shift is to bring the seasonal variations nearer to that of the mid- to high-latitude variations of the Garcia and Solomon (1985) model, whose temporal variations are illustrated in more detail in Pilinski and Crowley (2015). The shifted profile is illustrated in Figure 2 along with the Q09 profile, in addition to the

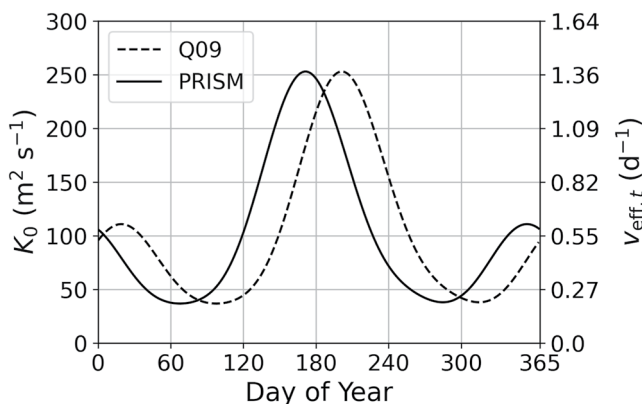


Figure 2. Seasonal variations of the eddy diffusion coefficient at $\sim 97 \text{ km}$ altitude applied at the lower boundary of the Thermosphere-Ionosphere-Electrodynamics General Circulation Model by Q09 (dashed line), and the 30-day shifted profile used by PRISM (solid line). The right-hand axis shows the effective Rayleigh friction coefficient calculated using Equation 2.

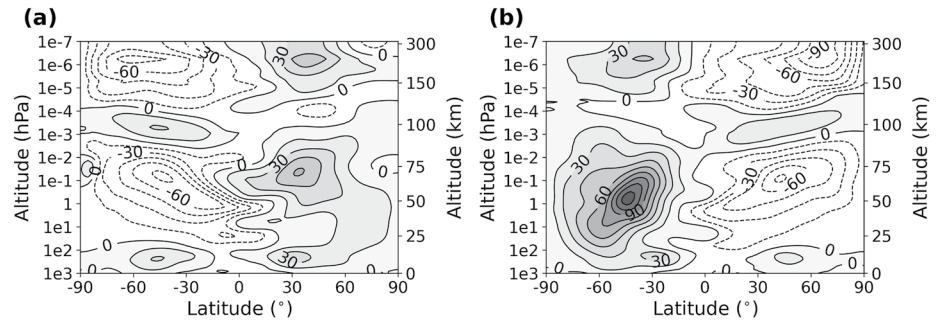


Figure 3. NAVHWER zonal mean zonal winds for January (a) and July (b) 2015 conditions. Contours show eastward (solid) and westward (dashed) winds spaced in 15 m s^{-1} intervals.

corresponding effective Rayleigh friction values calculated using Equation 2. The impact of eddy diffusion and of the 30-day shift are discussed in more detail in Section 4.

Following V86, molecular diffusion of momentum is parameterized as an effective Rayleigh friction using $v_{\text{eff},m}(z) = 5.28 \times 10^{-13} \exp[-z/7] \text{ s}^{-1}$, where z is in units of kilometer. In addition, following V86 a Prandtl number of 1 is assumed, which implies that the Rayleigh friction terms representing eddy and molecular diffusion of momentum are equally applied as Newtonian cooling terms for the eddy and molecular diffusion of heat.

Momentum sinks arising from turbulent surface fluxes and unresolved topography have often been parameterized as a Rayleigh friction term in coarse resolution general circulation models (e.g., McLandress, 2002; T. G. Shepherd et al., 1996; Stevens et al., 2002). In the current work, the surface Rayleigh friction profile from Chen et al. (2007) is adopted. This profile has a surface value of A_0 and decreases linearly in sigma-coordinates between $\sigma = 1$ and $\sigma = 0.7$ ($\sim 3 \text{ km}$ altitude). While Chen et al. (2007) consider values of A_0 in the range of $0.6\text{--}4.0 \text{ d}^{-1}$, a value of $A_0 = 3.0 \text{ d}^{-1}$ is employed in the current work. The model sensitivity to surface friction, as well as the choice of A_0 , is discussed in more detail in Section 4.

The 10 highest model levels ($\sim 300\text{--}430 \text{ km}$ altitude) act as a “sponge layer” to prevent spurious model top wave-reflections. For this, an altitude-dependent damping rate of $\alpha_s (1 + \tanh[(z - 250)/40])$ is applied to all dynamical fields, where $\alpha_s = 25 \text{ d}^{-1}$ and z is in units of kilometer.

2.3. Background Atmosphere

The mean zonal winds and temperatures of the background atmosphere can be freely specified in PRISM. This is achieved by relaxing the zonal mean spherical harmonic coefficients toward a zonal mean assimilation state, for which a nudging rate of $D = 1/3 \text{ d}^{-1}$ is used. Since only the zonal mean spherical harmonics are involved in the nudging, the simulated tides are not affected by this.

The mean zonal winds and temperatures in the middle atmosphere ($85\text{--}0.001 \text{ hPa}$) are nudged to daily mean zonal mean fields calculated from 3-hourly NAVGEM-HA data. NAVGEM-HA is a meteorological analysis system extending up to the lower thermosphere ($\sim 116 \text{ km}$), assimilating satellite observations of temperature, water vapor, and ozone in the Middle Atmosphere, as well as standard operational meteorological observations in the troposphere and stratosphere (McCormack et al., 2017). Seasonal and short-term variations in the NAVGEM-HA winds and temperatures have been shown to be in good agreement with independent satellite-based wind observations (Dhadly et al., 2018), and with ground-based meteor radar observations (Eckermann et al., 2018; Laskar et al., 2019; McCormack et al., 2017; Stober et al., 2020).

Between the surface and 85 hPa the mean zonal winds and temperatures are nudged to daily mean zonal mean fields calculated from the ERA5 reanalysis data set (Hersbach et al., 2020). Above 0.001 hPa , the assimilated fields are based on daily mean zonal mean zonal winds and temperatures from the empirical Horizontal Wind Model version 2014 (HWM14, Drob et al., 2015) and the NRLMSISE-00 reference model (Picone et al., 2002), respectively. In the following sections, the composite atmosphere between the surface and thermosphere is referred to as the NAVHWER atmosphere. The NAVHWER zonal mean zonal winds for January and July 2015 conditions are illustrated in Figure 3, up to the base of the sponge layer. Diagnostic simulations where the boundaries between

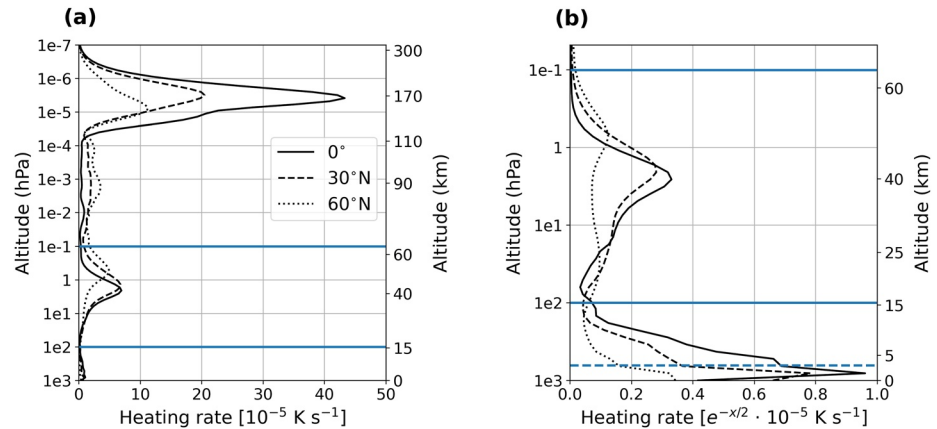


Figure 4. Vertical profiles of the migrating semidiurnal amplitude in the Specified Dynamics Whole Atmosphere Community Climate Model with Thermosphere and Ionosphere Extension temperature tendency fields for January 2015 at 0°, 30°, and 60° latitude (a). The amplitudes are scaled by a factor $\exp(-x/2)$ in panel (b), where $x = -\ln(p/p_0)$. The solid blue lines demarcate the boundaries of the tropospheric, stratospheric and mesosphere-thermosphere forcing regions referred to in the text. The dashed blue line indicates the upper boundary of surface friction.

the different data sets used to construct the NAVWHER atmosphere are artificially smoothed, find that any discontinuities which may be present between the data sets have a negligible impact on the simulated SW2 tide.

2.4. Tidal Forcing

The SW2 tide is forced by incorporating 3-hourly global temperature tendency fields ($K s^{-1}$), also referred to as heating rates, from the Specified Dynamics Whole Atmosphere Community Climate Model with Thermosphere Extension version 2.1 (SD-WACCMX, H.-L. Liu et al., 2018). SD-WACCMX is a comprehensive whole atmosphere-ionosphere numerical model extending from the surface up to 500–700 km altitude, where the winds and temperatures below ~ 50 km altitude are specified to data from the Modern-Era Retrospective analysis for Research and Applications Version 2 (MERRA-2, Gelaro et al., 2017). The SD-WACCMX model includes parameterizations of the major chemical and radiative processes between the troposphere and thermosphere, including those of the ionosphere and of non-local-thermal-equilibrium processes. The version of SD-WACCMX used in this study has a horizontal latitude-longitude resolution of 1.9 by 2.5°, with a vertical resolution between 1.0 and 3.5 km. All available SD-WACCMX temperature tendency fields are incorporated in the simulations presented in this work, which include the temperature tendencies due to shortwave radiation, longwave radiation, moist processes, NO cooling, and gravity wave dissipation.

To force the tides, the SD-WACCMX temperature tendencies are first interpolated from their native vertical hybrid sigma-pressure grid to the PRISM sigma-coordinate grid. These interpolated fields are then interpolated linearly in time onto the PRISM temperature tendency equation at timestep n for each model level l (represented by \dots), as

$$\frac{\partial \Theta_l^n}{\partial t} = \dots + \frac{\partial \Theta_l^n}{\partial t} \Big|_{\text{SD-WACCMX}} \quad (4)$$

As a result, the model time-integration step will then generate atmospheric heating and cooling in accordance with the prescribed SD-WACCMX temperature tendency fields. This in turn excites a broad spectrum of atmospheric buoyancy waves, including the thermal tides. While the current work focuses on the SW2 tide, the SD-WACCMX temperature tendencies in principle excite a full spectrum of migrating and non-migrating tides. Here we note that PRISM does not include any other parameterizations of diabatic processes.

Figure 4 shows the amplitude of the SW2 component of the SD-WACCMX temperature tendency fields (the “SW2 forcing”) for January 2015 conditions at 0°, 30°, and 60° latitude, calculated using 2D Fourier analysis. Figure 4a shows that the peak SW2 heating rates occur in the thermosphere, with a secondary peak located in the stratosphere. The forcing is generally stronger toward the equator. In Figure 4b the forcing has been scaled by a

factor $\exp(-x/2)$ following Forbes (1982), where $x = -\ln(p/p_0)$ and p_0 is the surface pressure. This scaling factor compares the relative importance of the forcing strength by altitude, by adjusting for the decreasing density of the atmosphere as it appears in the tidal equations (Chapman & Lindzen, 1970). As a result, the relative forcing strength becomes comparable between the troposphere and stratosphere regions, with that of the stratosphere peaking near 40 km and that of the troposphere peaking near the surface. In addition, the relative forcing strength is close to zero near to the tropopause (100 hPa), and converges to zero for altitudes around ~ 60 –65 km.

In Section 5 the distinction is made between the MLT amplitude of the SW2 tides forced in the troposphere, stratosphere, and MT regions. To that end, the solid blue lines in Figure 4 mark the altitude regions broadly encompassing the tropospheric forcing (1,000–100 hPa), the stratospheric forcing (100–0.1 hPa), and MT forcing (0.1– 10^{-7} hPa). The dotted blue line in Figure 4b indicates the highest altitude where surface friction applies.

2.5. SuperDARN Observations and Model Sampling

The 10 SuperDARN radars used in this study are the same as those used in the study of van Caspel et al. (2020), and span 180° of longitude around a 14° latitude band centered on 60° North. The SuperDARN radars make time-synchronized hourly horizontal wind measurements based on the back-scatter signal of meteor ablation trails in the MLT (Hussey et al., 2000). While a detailed description and validation of the method used to extract the SW2 tide from the array of SuperDARN measurements is given in van Caspel et al. (2020), a brief description of the method is included here.

The vertical distribution of meteor echoes observed in the first four range gates of the SuperDARN radars extends between 75 and 125 km altitude and is approximately a Gaussian centered on 100 km altitude with a Full Width at Half Maximum (FWHM) between 25 and 35 km (Chisham & Freeman, 2013). The average FWHM of the first four range gates as used in this study is approximately 30 km. The SW2 tidal signal is extracted from the hourly SuperDARN winds by least squares fitting a function representing the migrating diurnal, semidiurnal, and terdiurnal tide, including a mean wind, in both space and time to data from all stations. While van Caspel et al. (2020) employed a 10-day sliding window to perform the tidal fit, a 16-day window is used in the current work. This is done to reduce the impact of any possible lunar (12.42 hr) tide contamination (Maute et al., 2016; Sandford et al., 2006), and of low-frequency planetary wave modulation (Teitelbaum & Vial, 1991). Furthermore, because of the large number of data points included in each fit, the uncertainties on the fitted tidal parameters becomes negligibly small (less than 0.5 ms^{-1} and 20 min for the tidal amplitudes and phases, respectively) when taking into account the uncertainty estimates on the hourly SuperDARN winds.

To compare the model to observation, 3-hourly instantaneous PRISM output is first interpolated to the locations of available SuperDARN measurements. The sampled data are then interpolated to a 75–125 km altitude grid with 2.5 km spacing by numerically integrating the barometric formula. A SuperDARN “observational filter” is then applied to the interpolated data, represented by a Gaussian vertical averaging kernel following the SuperDARN meteor echo distribution. For this, a Gaussian centered on 100 km altitude with a FWHM of 30 km is used. We note that, while the mean height and FWHM of the SuperDARN meteor echo distribution can exhibit seasonal variations on the order of a few km (Chisham, 2018), such variations only minimally impact the SW2 simulation results.

In the following, the sampled and vertically averaged model winds are referred to as PRISM-SDARN. The model winds are analyzed using the same method used for the hourly SuperDARN winds, but now using a 16-day sliding window that is stepped forward in 3-hourly steps, to accommodate the temporal resolution of the model output.

3. Simulation Results

Figure 5 compares the PRISM-SDARN and observed SuperDARN SW2 tidal amplitude and phase for the year 2015, with reference to the climatological amplitude and phase based on observations between the years 2000 and 2016 (van Caspel et al., 2020). The tidal phases are expressed in terms of local time of maximum (hr), which for the migrating tides is independent of longitude.

The main seasonal characteristics of the observed tide are its amplitude maxima in September and in winter, and its rapid phase transitions coincident with amplitude minima in March and late October. These features show little year-to-year variability (van Caspel et al., 2020), and are consistent with numerous other northern hemisphere

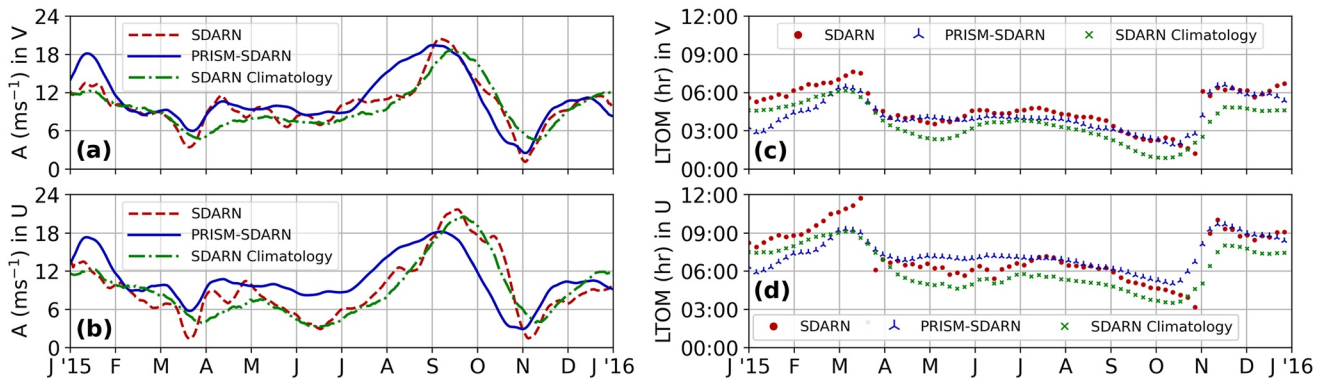


Figure 5. Simulated PRISM-SDARN (blue) and observed Super Dual Auroral Radar Network (SDARN, red) migrating semidiurnal amplitude and phase in the meridional (a, c) and zonal (b, d) wind for the year 2015, and the climatological observed amplitude and phase (green) based on observations between the years 2000 and 2016 (van Caspel et al., 2020).

observations of the mid- and high-latitude SW2 tide (e.g., He & Chau, 2019; Wu et al., 2011). Figure 5 demonstrates that the observed seasonal behavior of the SW2 amplitude and phase for the year 2015 are closely representative of the climatological seasonal variations.

The PRISM-SDARN simulation results display good year-round agreement with the observed tide, with all of the seasonal characteristics being well reproduced. For the tidal amplitudes, the largest discrepancies occur in January and between August and October. In January, the model overestimates amplitudes by up to 5 ms^{-1} , while between August–October amplitudes can differ by as much as 12 (6) ms^{-1} in the zonal (meridional) wind. The amplitude differences between August–October mostly represent variations in the temporal evolution of the September maximum. Another difference between model and observation is that the observed amplitudes are consistently smaller (greater) in the zonal wind than in the meridional in June (September; van Caspel et al., 2020), as can also be seen in Figure 5. In contrast, the modeled zonal and meridional amplitudes are nearly identical at all times.

For the tidal phases, the main discrepancy occurs between January and March. During this time, the modeled phase is approximately 2.5 hr earlier than observation. Nevertheless, the phases show excellent agreement during the rest of the year. By comparison of Figures 5d and 5c, it follows that both the simulated and observed tide display a circular phase relation, where the meridional component leads the zonal by approximately 3 hr.

The results from this section give confidence that the model adequately describes the main processes governing the seasonal variations of the SW2 tide. That is to say, that the tidal forcing scheme, background atmospheric specification, dissipation terms, and output sampling technique, are sufficiently realistic to reproduce the observed seasonal behavior of the tide. In the following section, numerical experiments are performed to investigate which aspects of the model most strongly control the simulation results.

4. Model Analysis

Numerical experiments are performed to investigate the impact of the background atmosphere, tidal forcing, eddy diffusion, and surface friction on the ability of the model to simulate the SW2 tide observed by SuperDARN. In these experiments, only the meridional component of the tide is considered, since it was established in the previous section that the modeled tide is circularly polarized but otherwise nearly identical between the zonal and meridional wind. We further note that the simulations presented in this work are insensitive to the specification of ion drag, molecular diffusion, and Newtonian cooling. A separate sensitivity study for these parameterizations is therefore not included. An overview of the numerical experiments of this section is given in Table 1.

4.1. Experiment Results

Figures 6a and 6d compare PRISM-SDARN against a simulation made using a zero-wind background atmosphere (ZeroWind). The background atmosphere of the ZeroWind experiment is constructed using a single global

Table 1
Numerical Experiment Design

Experiment	Configuration
PRISM-SDARN	Standard model configuration (see Section 2)
ZeroWind	As PRISM-SDARN, zero-wind background atmosphere
NoEdDiff	As PRISM-SDARN, no eddy diffusion
NoEdShift	As PRISM-SDARN, no 30-day shift Q09 eddy diffusion profile
SurfEnhan	As PRISM-SDARN, surface friction coefficient $A_0 = 4.5 \text{ d}^{-1}$
SurfReduc	As PRISM-SDARN, surface friction coefficient $A_0 = 1.5 \text{ d}^{-1}$

Note. SDARN, Super Dual Auroral Radar Network.

mean yearly mean vertical temperature profile, yielding zero zonal mean zonal winds everywhere. The amplitude and phase of the SW2 tide observed by SuperDARN are included here for reference.

In the ZeroWind simulation, the tidal phase and amplitude see little to no seasonal variation. As a result, it can be concluded that the NAVWHER atmosphere strongly impacts the simulated SW2 tide, giving rise to the seasonal phase characteristics and to the amplitude maxima in September and winter. The ZeroWind experiment also demonstrates that any seasonal variations in the tidal forcing itself only minimally impact the simulated tide.

Figures 6b and 6c compare PRISM-SDARN against simulations where the eddy diffusion has been turned off (NoEdDiff), and where the employed seasonal variations of Q09 have not been shifted forward by 30 days. The NoEdDiff experiment demonstrates that eddy diffusion primarily acts to damp the tide between March and mid-September and in December. This in turn contributes to the rapid amplitude increase toward the September maximum, which in the model falls broadly between August and September. The impact of eddy diffusion on the simulated tidal phase is very minimal. The NoEdShift experiment demonstrates that employing the global seasonal variations of Q09 without applying a 30-day shift toward the mid- to high-latitude variations of the Garcia and Solomon (1985) model, damps the tide less strongly between May and June, more strongly between July and September, and slightly less strongly in December. Here the changes between May-June and July-September represent especially strong departures from PRISM-SDARN and the (climatological) observed tide.

Figures 6c and 6f compare PRISM-SDARN against simulations where the surface friction coefficient has been reduced by a factor of 0.5 (SurfReduc), and where it has been enhanced by a factor of 1.5 (SurfEnhan). These

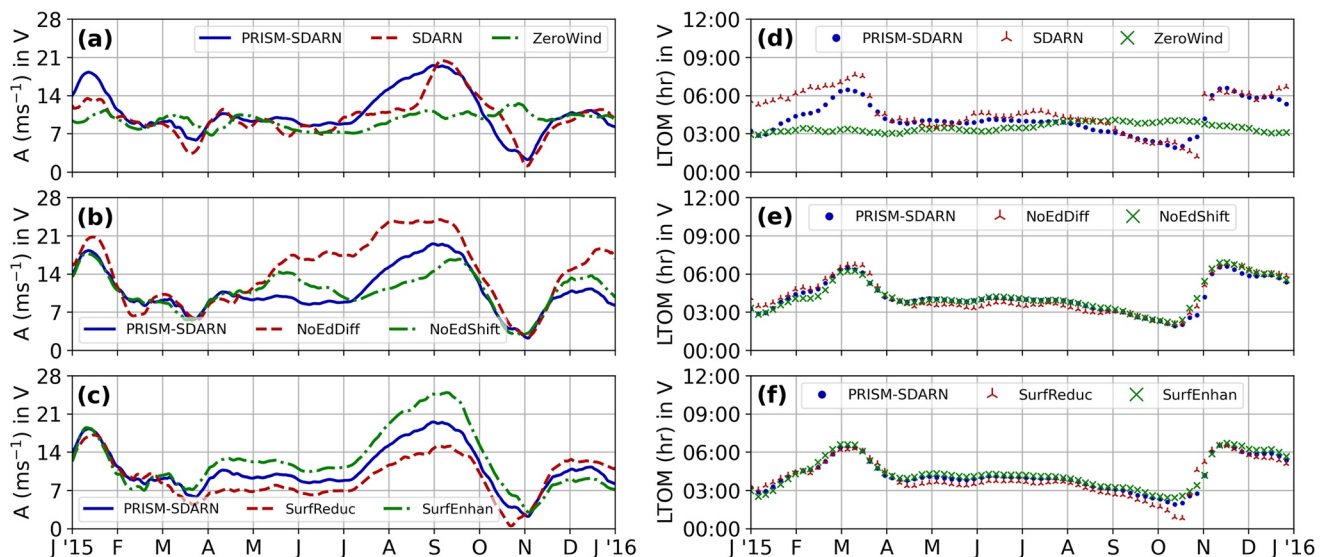


Figure 6. Meridional component of the migrating semidiurnal (SW2) observed by Super Dual Auroral Radar Network (SDARN) and the SW2 simulation results for the ZeroWind and PRISM-SDARN (a, d), NoEdDiff and NoEdShift (b, e), and SurfReduc and SurfEnhan (c, f) simulations as listed in Table 1.

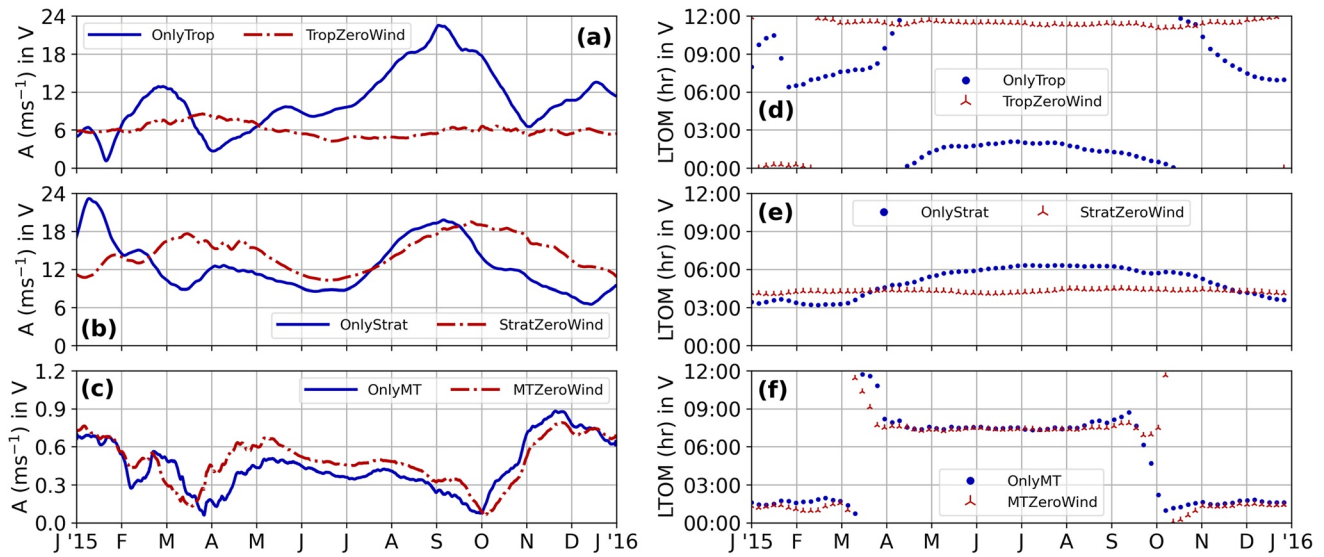


Figure 7. Meridional migrating semidiurnal forcing response for the OnlyTrop and TropZeroWind (a, d), OnlyStrat and StratZeroWind (b, e), and OnlyMT and MTZeroWind (c, f) numerical experiments. Note the different y-axis scaling in panel (c).

experiments demonstrate that the main impact of increased surface friction is to enhance the simulated amplitudes between April–October, with the enhancement being most pronounced between August–September. Furthermore, the amplitude increase shows an almost perfectly linear relationship with the strength of the surface friction coefficient A_0 . This relation is also confirmed in diagnostic simulations for values of A_0 outside of the range shown here, starting from zero and up to 10 d^{-1} . The simulated phase is impacted by surface friction to a lesser extent, but is generally delayed as surface friction increases. The yearly mean LTOM is 03:59, 04:09, and 04:18 hr for the SurfReduc, PRISM-SDARN, and SurfEnhan simulations, respectively. This delay is consistent with the results of Sakazaki and Hamilton (2017), who found a doubling of their specification of surface friction to delay the phase of the SW2 component of the surface tide by about 10 min. We further note that the impact of surface friction is not exclusive to the simulated SW2 tide observed by SuperDARN, but that the model indicates that it extends across the mid- and high-latitude MLT.

Diagnostic simulations without either surface friction or eddy diffusion also find the simulated magnitude of the August–September amplitude maximum to be substantially smaller than that of the observed tide. The inclusion of surface friction is therefore required to make the simulated amplitude match the observed September maximum. Owing to this sensitivity, the surface friction value of $A_0 = 3.0 \text{ d}^{-1}$ was determined to yield the best agreement with observation. This choice of A_0 does, however, fall well within the range of surface friction values described in literature. For example, Stevens et al. (2002) find a surface Rayleigh friction value of 1.9 d^{-1} over the tropical pacific ocean, while Yang et al. (2013) find surface Rayleigh friction values up to 5.5 d^{-1} over land.

5. Forcing Decomposition

To investigate the impact of the background atmosphere on the simulated SW2 tide in more detail, a distinction is made between the SW2 tide forced in the troposphere, stratosphere, and MT regions (see Section 2.4). This is motivated by the vertical propagation path to SuperDARN meteor echo heights (75–125 km) being considerably different for the tides forced within these regions. For example, the peak forcing altitude in the troposphere occurs near the surface, in the stratosphere near 40 km, and in the MT near 170 km (as shown in Figure 4). To compare the baseline effect on the forcing response from the different regions, Figure 7 compares the tropospheric (OnlyTrop), stratospheric (OnlyStrat), and MT (OnlyMT) SW2 forcing simulations against corresponding zero-wind tropospheric (TropZeroWind), stratospheric (StratZeroWind), and MT (MTZeroWind) simulations. An overview of these experiments is given in Table 2.

By comparison with the TropZeroWind simulations, the OnlyTrop experiment demonstrates that the seasonal variations of the NAVHWER atmosphere induce strong seasonal variations in both the amplitude and phase

Table 2
Forcing Decomposition Experiment Design

Experiment	Configuration
OnlyTrop	As PRISM-SDARN, tide forced only between 1,000–100 hPa
OnlyStrat	As PRISM-SDARN, tide forced only between 100–0.1 hPa
OnlyMT	As PRISM-SDARN, tide forced only between 0.1–10 ⁻⁷ hPa
TropZeroWind	As OnlyTrop, zero-wind background atmosphere
StratZeroWind	As OnlyStrat, zero-wind background atmosphere
MTZeroWind	As OnlyMT, zero-wind background atmosphere

Note. SDARN, Super Dual Auroral Radar Network.

of the tropospheric SW2 forcing response. The amplitude of the forcing response is enhanced by as much as a factor of 4, while a roughly bi-modal phase behavior is established between the summer and winter half-year. An exception to the latter occurs in January, when the phase is delayed coincident with a local amplitude minimum.

The stratospheric forcing response is comparatively less affected by the seasonal variations in the background atmosphere. The main amplitude enhancement occurs in January, with lower amplitudes during much of the rest of the year. The phase is delayed by 2.5 hr at most, and shows no signs of major seasonal variations. Further, while it is impossible to determine if the behavior of the stratospheric and tropospheric forcing response during January represents a seasonal effect or isolated event based on a 1-year simulation, it is interesting to note that January was marked by a minor sudden stratospheric warming event (Manney et al., 2015).

Both the amplitude and phase of the MT forcing response show a bi-modal seasonal behavior, which is largely unchanged between the OnlyMT and MTZeroWind simulations. The amplitudes broadly maximize during the summer and winter seasons, having minima in March and October. The bi-modal characteristics of the MT forcing response are reminiscent of the mid- to high-latitude structure of the SW2 forcing in the MLT described by Hagan (1996). There an anti-symmetric latitudinal structure in the SW2 tide forcing between summer and winter solstice is associated with changes in the forcing brought about by the secondary ozone maximum. Consistent with their results is that the MT forcing response in our simulations is entirely attributable to shortwave radiation effects. However, since the MT forcing response is comparatively insignificant relative to those of the troposphere and stratosphere, a more detailed investigation into its drivers is not included in the current work.

6. Conclusion and Discussion

This study uses a primitive equation model to simulate the SW2 tide observed by a longitudinal array of SuperDARN meteor radars for the year 2015, to mechanistically identify which processes contribute to the seasonal variations of the SW2 tide in the mid- to high-latitude MLT. The model convincingly reproduces the observed seasonal variations in the tidal amplitude and phase, which include amplitude maxima in September and in winter, and rapid phase transitions coincident with amplitude minima in March and October.

By comparison with zero-wind simulations, the seasonal characteristics of the SW2 tide are found to be shaped largely by the seasonal variations in the background atmosphere. While this result is consistent with literature (e.g., Hagan et al., 1999; Lindzen & Shung Hong, 1974), numerical experiments find it to be almost entirely attributable to the SW2 tide forced in the troposphere. The background atmosphere amplifies the amplitude of the tropospheric forcing response by as much as a factor of 4, while also giving rise to rapid phase transitions in March and April. In contrast, the amplitude of the stratospheric forcing response is impacted only by a factor of 0.8–0.9 throughout most of the year, while its phase displays no major seasonal variations. As a consequence of the tropospheric amplification, the contribution to the net simulated tide becomes comparable in magnitude between the tides forced in the troposphere and stratosphere regions, consistent with the results of Hagan (1996). The contribution to the net simulated tide by the tide forced in the mesosphere-thermosphere region is found to be much smaller, reaching an amplitude of at most 0.9 ms⁻¹.

Tidal damping by eddy diffusion is parameterized as a seasonally dependent effective Rayleigh friction. The primary effect of eddy diffusion is to reduce the simulated SW2 amplitudes by a factor of ~0.5 broadly around

summer solstice and in December. The tidal damping around summer solstice represents an important factor in bringing the model into agreement with observation. In simulations without eddy diffusion, the summertime amplitude maximum is much broader than observation, with amplitudes beginning to increase as early as May. Tidal dissipation by eddy diffusion may therefore be an important factor contributing to the summertime discrepancies between modeled and observed semidiurnal tides (e.g., Pancheva et al., 2020; Stober et al., 2020, 2021).

The specification of a narrow surface friction layer is found to increase the net amplitude of the simulated SW2 tide in the MLT between April and October. Especially the increased amplitudes between August and September represent an important factor in bringing the amplitude of the simulated tide in agreement with observation. Using diagnostic simulations where surface reflections are artificially removed, the effect of surface friction is identified as being caused by its dampening effect on the surface reflection of the tide. This in turn changes the complex interference pattern between the tides forced in the different source regions and their respective surface reflections. Given the implications of surface friction as a coupling mechanism between the boundary layer and semidiurnal tidal variability in the MLT, the mechanism and impact of surface friction will be investigated in more detail in a future study by means of a Hough-mode decomposition. In addition, future efforts can focus on the implementation of a more realistic spatially and temporally varying implementation of surface friction. This would include, for example, longitudinal ocean and land contrasts (Chiang & Zebiak, 2000; Yang et al., 2013). Based on our results for the SW2 tide, we anticipate that surface friction may serve as a possible excitation mechanism for non-migrating semidiurnal tides. A more realistic specification of surface friction would also include different zonal and meridional surface friction coefficients (Stevens et al., 2002). The lack of such a distinction may be a factor contributing to the simulated tide having the same amplitude in the zonal and meridional wind, whereas the observed tides frequently show different amplitudes.

Data Availability Statement

SuperDARN data are available from Virginia Tech at <http://vt.superdarn.org/tiki-index.php>, last access: September 2021. SD-WACCMX data are available at <https://www.earthsystemgrid.org> CCSM run SD-WACCM-X v2.1, Atmosphere History Data, 3-Hourly Instantaneous Values, version 7, last access: September 2021.

Acknowledgments

The current research was supported by the Research Council of Norway (grant no. 223525/F50). The authors acknowledge the use of NAVGEM-HA data and SuperDARN meteor wind data. Development of NAVGEM-HA was supported by the Chief of Naval Research and the Department of Defense High Performance Computing Modernization Project. The SuperDARN project is funded by national scientific funding agencies of Australia, China, Canada, France, Japan, Italy, Norway, South Africa, the United Kingdom, and the United States. The authors are deeply indebted to R. S. Lieberman, whose kindness and support made the modeling aspect of this work possible. We also thank the support from the NASA TIMED program.

References

- Arras, C., Jacobi, C., & Wickert, J. (2009). Semidiurnal tidal signature in sporadic occurrence rates derived from GPS radio occultation measurements at higher midlatitudes. *Annales Geophysicae*, 27(6), 2555–2563. <https://doi.org/10.5194/angeo-27-2555-2009>
- Becker, E. (2017). Mean-flow effects of thermal tides in the mesosphere and lower thermosphere. *Journal of the Atmospheric Sciences*, 74(6), 2043–2063. <https://doi.org/10.1175/JAS-D-16-0194.1>
- Chapman, S., & Lindzen, R. S. (1970). *Atmospheric tides*. Springer Netherlands. <https://doi.org/10.1007/978-94-010-3399-2>
- Chen, G., Held, I. M., & Robinson, W. A. (2007). Sensitivity of the latitude of the surface westerlies to surface friction. *Journal of the Atmospheric Sciences*, 64(8), 2899–2915. <https://doi.org/10.1175/jas3995.1>
- Chiang, J. C. H., & Zebiak, S. E. (2000). Surface wind over tropical oceans: Diagnosis of the momentum balance, and modeling the linear friction coefficient. *Journal of Climate*, 13(10), 1733–1747. [https://doi.org/10.1175/1520-0442\(2000\)013<1733:swotod>2.0.co;2](https://doi.org/10.1175/1520-0442(2000)013<1733:swotod>2.0.co;2)
- Chisham, G. (2018). Calibrating SuperDARN interferometers using meteor backscatter. *Radio Science*, 53(6), 761–774. <https://doi.org/10.1029/2017rs006492>
- Chisham, G., & Freeman, M. P. (2013). A reassessment of SuperDARN meteor echoes from the upper mesosphere and lower thermosphere. *Journal of Atmospheric and Solar-Terrestrial Physics*, 102, 207–221. <https://doi.org/10.1016/j.jastp.2013.05.018>
- Conte, J. F., Chau, J. L., Laskar, F. I., Stober, G., Schmidt, H., & Brown, P. (2018). Semidiurnal solar tide differences between fall and spring transition times in the northern hemisphere. *Annales Geophysicae*, 36(4), 999–1008. <https://doi.org/10.5194/angeo-36-999-2018>
- Dhadly, M. S., Emmert, J. T., Drob, D. P., McCormack, J. P., & Niciejewski, R. J. (2018). Short-term and interannual variations of migrating diurnal and semidiurnal tides in the mesosphere and lower thermosphere. *Journal of Geophysical Research: Space Physics*, 123(8), 7106–7123. <https://doi.org/10.1029/2018ja025748>
- Drob, D. P., Emmert, J. T., Meriwether, J. W., Makela, J. J., Doornbos, E., Conde, M., et al. (2015). An update to the horizontal wind model (HWM): The quiet time thermosphere. *Earth and Space Science*, 2(7), 301–319. <https://doi.org/10.1002/2014ea000089>
- Eckermann, S. D., Ma, J., Hoppel, K. W., Kuhl, D. D., Allen, D. R., Doyle, J. A., et al. (2018). High-altitude (0–100 km) global atmospheric reanalysis system: Description and application to the 2014 austral winter of the deep propagating gravity wave experiment (DEEPWAVE). *Monthly Weather Review*, 146(8), 2639–2666. <https://doi.org/10.1175/mwr-d-17-0386.1>
- Forbes, J. M. (1982). Atmospheric tide: 2. The solar and lunar semidiurnal components. *Journal of Geophysical Research*, 87(A7), 5241–5252. <https://doi.org/10.1029/ja087ia07p05241>
- Forbes, J. M. (2009). Vertical coupling by the semidiurnal tide in Earth's atmosphere. In T. Tsuda, R. Fujii, K. Shibata, & M. A. Geller (Eds.), *Climate and weather of the Sun-Earth system (CAWSES): Selected papers from the 2007 Kyoto Symposium* (pp. 337–348). TERRAPUB.
- Forbes, J. M., & Garrett, H. B. (1979). Theoretical studies of atmospheric tides. *Reviews of Geophysics*, 17(8), 1951–1981. <https://doi.org/10.1029/RG017i008p01951>
- Forbes, J. M., Roble, R. G., & Fesen, C. G. (1993). Acceleration, heating, and compositional mixing of the thermosphere due to upward propagating tides. *Journal of Geophysical Research*, 98(A1), 311–321. <https://doi.org/10.1029/92JA00442>

- Forbes, J. M., & Vincent, R. A. (1989). Effects of mean winds and dissipation on the diurnal propagating tide: An analytic approach. *Planetary and Space Science*, 37(2), 197–209. [https://doi.org/10.1016/0032-0633\(89\)90007-X](https://doi.org/10.1016/0032-0633(89)90007-X)
- Garcia, R. R., & Solomon, S. (1985). The effect of breaking gravity waves on the dynamics and chemical composition of the mesosphere and lower thermosphere. *Journal of Geophysical Research*, 90(D2), 3850–3868. <https://doi.org/10.1029/JD090iD02p03850>
- Gelaro, R., McCarty, W., Suárez, M. J., Todling, R., Molod, A., Takacs, L., et al. (2017). The modern-era retrospective analysis for research and applications, version 2 (MERRA-2). *Journal of Climate*, 30(14), 5419–5454. <https://doi.org/10.1175/jcli-d-16-0758.1>
- Hagan, M. E. (1996). Comparative effects of migrating solar sources on tidal signatures in the middle and upper atmosphere. *Journal of Geophysical Research*, 101(D16), 21213–21222. <https://doi.org/10.1029/96jd01374>
- Hagan, M. E., Burrage, M. D., Forbes, J. M., Hackney, J., Randel, W. J., & Zhang, X. (1999). GSWM-98: Results for migrating solar tides. *Journal of Geophysical Research*, 104(A4), 6813–6827. <https://doi.org/10.1029/1998ja900125>
- Hagan, M. E., Forbes, J. M., & Vial, F. (1993). Numerical investigation of the propagation of the quasi-two-day wave into the lower thermosphere. *Journal of Geophysical Research*, 98(D12), 23193–23205. <https://doi.org/10.1029/93JD02779>
- Hagan, M. E., Forbes, J. M., & Vial, F. (1995). On modeling migrating solar tides. *Geophysical Research Letters*, 22(8), 893–896. <https://doi.org/10.1029/95GL00783>
- He, M., & Chau, J. L. (2019). Mesospheric semidiurnal tides and near-12 h waves through jointly analyzing observations of five specular meteor radars from three longitudinal sectors at boreal midlatitudes. *Atmospheric Chemistry and Physics*, 19(9), 5993–6006. <https://doi.org/10.5194/acp-19-5993-2019>
- Hersbach, H., Bell, B., Berrisford, P., Hirahara, S., Horányi, A., Muñoz-Sabater, J., et al. (2020). The ERA5 global reanalysis. *Quarterly Journal of the Royal Meteorological Society*, 146(730), 1999–2049. <https://doi.org/10.1002/qj.3803>
- Holton, J. R. (2003). *An introduction to dynamic meteorology* (4th ed.). Academic Press.
- Hong, S.-S., & Lindzen, R. S. (1976). Solar semidiurnal tide in the thermosphere. *Journal of the Atmospheric Sciences*, 33(1), 135–153. [https://doi.org/10.1175/1520-0469\(1976\)033<0135:ssstitt>2.0.co;2](https://doi.org/10.1175/1520-0469(1976)033<0135:ssstitt>2.0.co;2)
- Hussey, G. C., Meek, C. E., André, D., Manson, A. H., Sofko, G. J., & Hall, C. M. (2000). A comparison of northern hemisphere winds using SuperDARN meteor trail and mf radar wind measurements. *Journal of Geophysical Research*, 105(D14), 18053–18066. <https://doi.org/10.1029/2000JD900272>
- Laskar, F. I., McCormack, J. P., Chau, J. L., Pallamraju, D., Hoffmann, P., & Singh, R. P. (2019). Interhemispheric meridional circulation during sudden stratospheric warming. *Journal of Geophysical Research: Space Physics*, 124(8), 7112–7122. <https://doi.org/10.1029/2018ja026424>
- Lieberman, R. S., France, J., Ortland, D. A., & Eckermann, S. D. (2021). The role of inertial instability in cross-hemispheric coupling. *Journal of the Atmospheric Sciences*, 78(4), 1113–1127. <https://doi.org/10.1175/JAS-D-20-0119.1>
- Lieberman, R. S., Riggin, D. M., Ortland, D. A., Oberheide, J., & Siskind, D. E. (2015). Global observations and modeling of nonmigrating diurnal tides generated by tide-planetary wave interactions. *Journal of Geophysical Research: Atmospheres*, 120(22), 11419–11437. <https://doi.org/10.1002/2015JD023739>
- Lindzen, R. S., & shung Hong, S. (1974). Effects of mean winds and horizontal temperature gradients on solar and lunar semidiurnal tides in the atmosphere. *Journal of the Atmospheric Sciences*, 31(5), 1421–1446. [https://doi.org/10.1175/1520-0469\(1974\)031<1421:eomwah>2.0.co;2](https://doi.org/10.1175/1520-0469(1974)031<1421:eomwah>2.0.co;2)
- Liu, G., Lieberman, R. S., Harvey, V. L., Pedatella, N. M., Oberheide, J., Hibbins, R. E., et al. (2021). Tidal variations in the mesosphere and lower thermosphere before, during, and after the 2009 sudden stratospheric warming. *Journal of Geophysical Research: Space Physics*, 126(3), e2020JA028827. <https://doi.org/10.1029/2020JA028827>
- Liu, H.-L., Bardeen, C. G., Foster, B. T., Lauritzen, P., Liu, J., Lu, G., et al. (2018). Development and validation of the whole atmosphere community climate model with thermosphere and ionosphere extension (WACCM-x 2.0). *Journal of Advances in Modeling Earth Systems*, 10(2), 381–402. <https://doi.org/10.1002/2017ms001232>
- Manney, G. L., Lawrence, Z. D., Santee, M. L., Read, W. G., Livesey, N. J., Lambert, A., et al. (2015). A minor sudden stratospheric warming with a major impact: Transport and polar processing in the 2014/2015 Arctic winter. *Geophysical Research Letters*, 42(18), 7808–7816. <https://doi.org/10.1002/2015GL065864>
- Manson, A. H., Meek, C., Hagan, M., Koshyk, J., Franke, S., Fritts, D., et al. (2002). Seasonal variations of the semi-diurnal and diurnal tides in the MLT: Multi-year MF radar observations from 2–70°n, modelled tides (GSWM, CMAM). *Annales Geophysicae*, 20(5), 661–677. <https://doi.org/10.5194/angeo-20-661-2002>
- Maute, A., Fejer, B. G., Forbes, J. M., Zhang, X., & Yudin, V. (2016). Equatorial vertical drift modulation by the lunar and solar semidiurnal tides during the 2013 sudden stratospheric warming. *Journal of Geophysical Research: Space Physics*, 121(2), 1658–1668. <https://doi.org/10.1002/2015JA022056>
- McCormack, J. P., Harvey, V. L., Pedatella, N., Koshin, D., Sato, K., Coy, L., et al. (2021). Intercomparison of middle atmospheric meteorological analyses for the northern hemisphere winter 2009–2010. *Atmospheric Chemistry and Physics Discussions*, 2021, 1–48. <https://doi.org/10.5194/acp-2021-224>
- McCormack, J. P., Hoppel, K., Kuhl, D., de Wit, R., Stober, G., Espy, P., et al. (2017). Comparison of mesospheric winds from a high-altitude meteorological analysis system and meteor radar observations during the boreal winters of 2009–2010 and 2012–2013. *Journal of Atmospheric and Solar-Terrestrial Physics*, 154, 132–166. <https://doi.org/10.1016/j.jastp.2016.12.007>
- McLandress, C. (2002). The seasonal variation of the propagating diurnal tide in the mesosphere and lower thermosphere. Part ii: The role of tidal heating and zonal mean winds. *Journal of the Atmospheric Sciences*, 59(5), 907–922. [https://doi.org/10.1175/1520-0469\(2002\)059<0907:tsvotp>2.0.co;2](https://doi.org/10.1175/1520-0469(2002)059<0907:tsvotp>2.0.co;2)
- Ortland, D. A. (2017). Daily estimates of the migrating tide and zonal mean temperature in the mesosphere and lower thermosphere derived from SABER data. *Journal of Geophysical Research: Atmospheres*, 122(7), 3754–3785. <https://doi.org/10.1002/2016jd025573>
- Ortland, D. A., & Alexander, M. J. (2006). Gravity wave influence on the global structure of the diurnal tide in the mesosphere and lower thermosphere. *Journal of Geophysical Research*, 111(A10). <https://doi.org/10.1029/2005JA011467>
- Ortland, D. A., & Alexander, M. J. (2014). The residual-mean circulation in the tropical tropopause layer driven by tropical waves. *Journal of the Atmospheric Sciences*, 71(4), 1305–1322. <https://doi.org/10.1175/JAS-D-13-0100.1>
- Ortland, D. A., Alexander, M. J., & Grimsdell, A. W. (2011). On the wave spectrum generated by tropical heating. *Journal of the Atmospheric Sciences*, 68(9), 2042–2060. <https://doi.org/10.1175/2011JAS3718.1>
- Pancheva, D., Mukhtarov, P., Hall, C., Meek, C., Tsutsumi, M., Pedatella, N., & Nozawa, S. (2020). Climatology of the main (24-h and 12-h) tides observed by meteor radars at Svalbard and Tromsø: Comparison with the models CMAM-DAS and WACCM-X. *Journal of Atmospheric and Solar-Terrestrial Physics*, 207, 105339. <https://doi.org/10.1016/j.jastp.2020.105339>
- Pedatella, N. M., & Forbes, J. M. (2010). Evidence for stratosphere sudden warming-ionosphere coupling due to vertically propagating tides. *Geophysical Research Letters*, 37(11). <https://doi.org/10.1029/2010GL043560>

- Pedatella, N. M., Liu, H.-L., Conte, J. F., Chau, J. L., Hall, C., Jacobi, C., et al. (2020). Migrating semidiurnal tide during the September equinox transition in the northern hemisphere. *Journal of Geophysical Research: Atmospheres*, e2020JD033822. <https://doi.org/10.1029/2020JD033822>
- Picone, J. M., Hedin, A. E., Drob, D. P., & Aikin, A. C. (2002). NRLMSISE-00 empirical model of the atmosphere: Statistical comparisons and scientific issues. *Journal of Geophysical Research*, 107(A12), SIA15–1–SIA15–16. <https://doi.org/10.1029/2002ja009430>
- Pilinski, M. D., & Crowley, G. (2015). Seasonal variability in global eddy diffusion and the effect on neutral density. *Journal of Geophysical Research: Space Physics*, 120(4), 3097–3117. <https://doi.org/10.1002/2015JA021084>
- Qian, L., Solomon, S. C., & Kane, T. J. (2009). Seasonal variation of thermospheric density and composition. *Journal of Geophysical Research*, 114(A1). <https://doi.org/10.1029/2008JA013643>
- Sakazaki, T., & Hamilton, K. (2017). Physical processes controlling the tide in the tropical lower atmosphere investigated using a comprehensive numerical model. *Journal of the Atmospheric Sciences*, 74(8), 2467–2487. <https://doi.org/10.1175/jas-d-17-0080.1>
- Sandford, D. J., Muller, H. G., & Mitchell, N. J. (2006). Observations of lunar tides in the mesosphere and lower thermosphere at arctic and middle latitudes. *Atmospheric Chemistry and Physics*, 6(12), 4117–4127. <https://doi.org/10.5194/acp-6-4117-2006>
- Shepherd, G., Roble, R. G., Zhang, S.-P., McLandress, C., & Wiens, R. H. (1998). Tidal influence on midlatitude airglow: Comparison of satellite and ground-based observations with time-GCM predictions. *Journal of Geophysical Research*, 103(A7), 14741–14751. <https://doi.org/10.1029/98JA00884>
- Shepherd, T. G., Semeniuk, K., & Koshyk, J. (1996). Sponge layer feedbacks in middle-atmosphere models. *Journal of Geophysical Research*, 101(D18), 23447–23464. <https://doi.org/10.1029/96JD01994>
- Smith, A. K. (2012). Global dynamics of the MLT. *Surveys in Geophysics*, 33(6), 1177–1230. <https://doi.org/10.1007/s10712-012-9196-9>
- Stevens, B., Duan, J., McWilliams, J. C., Münich, M., & Neelin, J. D. (2002). Entrainment, Rayleigh friction, and boundary layer winds over the tropical pacific. *Journal of Climate*, 15(1), 30–44. [https://doi.org/10.1175/1520-0442\(2002\)015<0030:erfabl>2.0.co;2](https://doi.org/10.1175/1520-0442(2002)015<0030:erfabl>2.0.co;2)
- Stober, G., Baumgarten, K., McCormack, J. P., Brown, P., & Czarnecki, J. (2020). Comparative study between ground-based observations and NAVGEM-HA analysis data in the mesosphere and lower thermosphere region. *Atmospheric Chemistry and Physics*, 20(20), 11979–12010. <https://doi.org/10.5194/acp-20-11979-2020>
- Stober, G., Kuchar, A., Pokhotelov, D., Liu, H., Liu, H.-L., Schmidt, H., et al. (2021). Interhemispheric differences of mesosphere/lower thermosphere winds and tides investigated from three whole atmosphere models and meteor radar observations. *Atmospheric Chemistry and Physics Discussions*, 1–50. <https://doi.org/10.5194/acp-2021-142>
- Teitelbaum, H., & Vial, F. (1991). On tidal variability induced by nonlinear interaction with planetary waves. *Journal of Geophysical Research*, 96(A8), 14169–14178. <https://doi.org/10.1029/91JA01019>
- van Caspel, W. E., Espy, P. J., Hibbins, R. E., & McCormack, J. P. (2020). Migrating tide climatologies measured by a high-latitude array of SuperDARN HF radars. *Annales Geophysicae*, 38(6), 1257–1265. <https://doi.org/10.5194/angeo-38-1257-2020>
- Vial, F. (1986). Numerical simulations of atmospheric tides for solstice conditions. *Journal of Geophysical Research*, 91(A8), 8955. <https://doi.org/10.1029/ja091ia08p08955>
- Wood, A. R., & Andrews, D. G. (1997). A spectral model for simulation of tides in the middle atmosphere. III: Results for the semidiurnal tide. *Journal of Atmospheric and Solar-Terrestrial Physics*, 59(1), 79–97. [https://doi.org/10.1016/1364-6826\(95\)00188-3](https://doi.org/10.1016/1364-6826(95)00188-3)
- Wu, Q., Ortland, D., Solomon, S., Skinner, W., & Niciejewski, R. (2011). Global distribution, seasonal, and inter-annual variations of mesospheric semidiurnal tide observed by TIMED TIDI. *Journal of Atmospheric and Solar-Terrestrial Physics*, 73(17), 2482–2502. <https://doi.org/10.1016/j.jastp.2011.08.007>
- Yang, W., Seager, R., & Cane, M. A. (2013). Zonal momentum balance in the tropical atmospheric circulation during the global monsoon mature months. *Journal of the Atmospheric Sciences*, 70(2), 583–599. <https://doi.org/10.1175/jas-d-12-0140.1>
- Zhang, J., Limpasuvan, V., Orsolini, Y. J., Espy, P. J., & Hibbins, R. E. (2021). Climatological westward-propagating semidiurnal tides and their composite response to sudden stratospheric warmings in SuperDARN and SD-WACCM-X. *Journal of Geophysical Research: Atmospheres*, 126(3), e2020JD032895. <https://doi.org/10.1029/2020JD032895>